Supplements

Texts:

Text S1: Tropospheric ozone trend analysis

Data:

To gain insight into the MERRA2-GMI tropospheric ozone columns trends, we employ a data product created from OMI and Microwave Limb Sounder (MLS) data that spans a latitude range of 60ºS-60ºN. Ziemke et al. (2006) employed a technique wherein tropospheric ozone columns were derived by subtracting MLS stratospheric columns from OMI total columns for each grid point daily. The precision of this dataset is estimated to be 1.3 DU. A comparison of these observations with ozonesondes for the period 2004-2005 yielded an RMSE value near 5 DU (Ziemke et al. 2006). It is worth noting that Ziemke et al. (2019) have observed a moderate drift (-1.0 DU/decade) caused by the row anomaly, which is currently being corrected for. This product does not follow an optimal estimation method to provide its dependency on the prior profiles (i.e., averaging kernels); therefore, we do not use this product to constrain our model.

Analysis:

In this study, despite the absence of observational constraints on tropospheric ozone concentrations from satellites in our study, it is deemed essential to provide insights into the long-term trends of MERRA2-GMI and their comparison with OMI/MLS observations. Here, we use daily-averaged MERRA2-GMI data without enforcing any masks used for OMI/MLS observations. The statistical significance of the linear trend maps of tropospheric ozone columns observed by OMI/MLS from 2005 to 2019 and simulated by MERRA2-GMI are depicted in Figure S3. OMI/MLS demonstrates a widespread increase in tropospheric ozone concentrations (+1-3 DU/decade) across the globe. The analysis shows that the increases in tropospheric ozone concentrations are more prominent in the northern hemisphere than in the southern hemisphere. The upward ozone trends are mainly concentrated in Asia due to a rise in anthropogenic emissions. The impact of Asian emissions on ozone pollution is not limited to its own region as it can transport hemispherically to the western United States, thereby increasing the background concentration levels (Cooper et al., 2010; Lin et al., 2017). The OMI/MLS trend map over the Pacific Ocean illustrates this observation clearly. The observations by OMI/MLS also indicate a hotspot of increased ozone concentrations over the subtropical Atlantic Ocean, which is potentially due to African biomass burning activities (Cuevas et al., 2013). The comparison of the OMI/MLS and MERRA2-GMI datasets indicates a strong degree of agreement in the northern hemisphere. Gaudel et al. (2018) have compiled long-term mountaintop nighttime ozone measurements in the northern hemisphere and found that most of them exhibit upward trends, representative of the free-tropospheric trends.

The trends observed in the southern hemisphere by OMI/MLS do not align with those simulated by MERRA2-GMI (Ziemke et al., 2019). Lu et al. (2019) indirectly supports the upward trends detected by OMI/MLS by compiling long-term records (1990-2015) of several surface observations and ozonesonde measurements at high latitudes in the southern hemisphere. Using a global model, they hypothesized that the upward trends may resulted from the expansion of Hadley circulation, particularly in austral autumn (March until May), leading to greater stratospheric contributions to the surface and a more effective mixing of ozone precursors from heavily polluted tropical regions to the free troposphere. However, it remains unverified whether this expansion occurs throughout the year, resulting in widespread upward trends observed by OMI/MLS. A more recent study, Thompson et al. (2021), utilized Southern Hemisphere Additional Ozonesondes (SHADOZ) data and suggested that the free-tropospheric ozone trends in 1998-2019 were fainter than those detected by satellite observations and varied greatly from season to season due to atmospheric dynamics (i.e., expansion or shrink in the tropopause height). An important caveat to consider is that satellite-based tropospheric ozone concentration can be largely uncertain due to limited sensitivity of the observed radiance to the optical path of ozone in the lower tropospheric region. Gaudel et

al. (2018) have compiled the tropospheric ozone trends observed by different satellites and retrieval algorithms and observed that most of them support the upward trends in Asia. However, there is vast disagreement when it comes to the southern hemisphere. Therefore, there is rather insufficient evidence to support the strong upward trends detected by OMI/MLS in the southern hemisphere, nor can it be claimed that MERRA2-GMI has reproduced reasonable trends in that region.

Text S2: Time series of tropospheric NO_2 columns

Figure S4 shows the long-term records of tropospheric NO_2 columns observed by OMI contrasted with those simulated by the MERRA2-GMI model, both pre- and post-application of the OI algorithm, over various areas. Regions undergoing statistically significant upwards trends are in the Middle East, India, and China. However, the recent reduced NOx emissions in China imposed since 2010-2012 are noticeable in the OMI time series. Particularly, the prior GMI simulation overestimates the upward trend due to lack of accounting for the recent emissions reduction. Both the U.S. and Europe have experienced an improvement in air quality with respect to NO_2 concentrations. OMI does not indicate any statistically significant changes in NO_2 over Canada which can be attributed to few OMI samples or increased emissions from the Canadian oil sands (McLinden et al., 2016) counteracting with improved mobile emissions in cities.

Text S3: Time series of total HCHO columns

Figure S6 shows the long-term time series of HCHO columns derived from OMI, the a priori-, and the a posteriori-MERRA2-GMI in 2005-2019 over a handful of regions. MERRA2-GMI largely overestimates summertime HCHO columns in the southeast US and Amazon Basin possibly due to uncertainties associated with the biogenic emissions. The posterior estimate corrects for the spuriously positive trends in HCHO over several parts of Amazon Basin not being supported by OMI observations (De Smedt et al., 2015). The a priori tends to underestimate the upward trends in HCHO over India, but it has high level of proficiency at capturing those over China and Middle East.

Text S4: The effect of OMI adjustments on XCH4

The temporal and spatial variations in the TOH changes should have non-uniform effects CH_4 concentrations given the fact that their emissions are not uniformly distributed. Figure 7 shows column-averaged mixing ratios of CH_4 (XCH_4) for the fifteen-year period (2005-2019) resulting from changes in TOH based on *SOMInitro*, *SOMIform*, and *SOMInitroform*, along with averaged XCH_4 from *Sbase*. The comparison of surface CH_4 observations from the US National Oceanic and Atmospheric Administration (NOAA) surface flasks (https://gml.noaa.gov/ccgg/about.html, last accessed: September 28, 2023) with simulations derived from *Sbase* shows a strong degree of correlation (r=0.90) (Figure S9), primarily attributed to the model's ability at accurately representing CH_4 seasonal cycles across the globe (Figure S10 and S11). However, the model overestimates global CH_4 by 3.3%, potentially due to biases associated with the bottom-up emissions. When summing CH_4 emissions in 2008-2017 to compare our bottom-up emissions to those reported in Saunois et al. (2020), we found our bottom-up emissions to have a global average of 717 Tg/yr, which is well within the range of reported values (594–881 Tg/yr). Nonetheless, Saunois et al. (2020) suggested that the top-down estimates might be lower than the bottom-up emission inventories, partly explaining our simulations being biased high.

The global reduction in TOH results in an increase in XCH4 across all seasons (Figure S12). The deviation in changes in XCH_4 is relatively consistent across the globe for the same reason. Nonetheless, XCH_4 tends to enhance more significantly over Africa where both CH_4 emissions and changes in TOH (~20%) are relatively large throughout the year. We observe a modest global deviation in changes in XCH_4 among seasons from this experiment (0.3 ppbv), with a peak in SON due to the global average XCH_4 being 0.4% (~7 ppbv) larger compared to the annual mean. Results obtained from *SOMIform* show a marginal increase in XCH_4 over tropics where OMI increments reduced TOH. This suggests that the OMI HCHO adjustments do not have a major influence on XCH_4. *SOMInitroform* leads to a relatively linear summation of two previous experiments.

Text S5: The effect of OMI adjustments on XCO

Figure S14 illustrates the effect of adjusted TOH on column-averaged mixing ratios of CO (XCO) for the fifteen-year period (2005-2019) based on the three experiments in addition to *Sanalysis*. A

comprehensive validation of CO concentrations in various domains including at the surface, integrated total columns, and profiles derived from in-situ and satellite observations, show a good degree of agreement (r>0.8) with consistent small biases (<10%) (Figure S15-20). The OMI NO_2 adjustments results in XCO enhancements due to the reduced TOH. The XCO enhancements are more local than those of XCH_4 due to the shorter CO lifetime. The enhancements reach above 10 ppbv in Africa. However, they quickly fade away in areas where the TOH changes are small. Similarly, the effect of reduced TOH on XCO did not lead to a noticeable long-term trend. Expectedly, the OMI HCHO adjustments do not lead to noticeable changes in XCO.

References:

Cooper, O.R., Gao, R.-S., Tarasick, D., Leblanc, T., Sweeney, C., 2012. Long-term ozone trends at rural ozone monitoring sites across the United States, 1990–2010. Journal of Geophysical Research: Atmospheres 117. https://doi.org/10.1029/2012JD018261

Cuevas, E., González, Y., Rodríguez, S., Guerra, J.C., Gómez-Peláez, A.J., Alonso-Pérez, S., Bustos, J., Milford, C., 2013. Assessment of atmospheric processes driving ozone variations in the subtropical North Atlantic free troposphere. Atmospheric Chemistry and Physics 13, 1973–1998. https://doi.org/10.5194/acp-13-1973-2013

De Smedt, I., Stavrakou, T., Hendrick, F., Danckaert, T., Vlemmix, T., Pinardi, G., Theys, N., Lerot, C., Gielen, C., Vigouroux, C., Hermans, C., Fayt, C., Veefkind, P., Müller, J.-F., Van Roozendael, M., 2015. Diurnal, seasonal and long-term variations of global formaldehyde columns inferred from combined OMI and GOME-2 observations. Atmospheric Chemistry and Physics 15, 12519–12545. https://doi.org/10.5194/acp-15-12519-2015

Gaudel, A., Cooper, O.R., Ancellet, G., Barret, B., Boynard, A., Burrows, J.P., Clerbaux, C., Coheur, P.-F., Cuesta, J., Cuevas, E., Doniki, S., Dufour, G., Ebojie, F., Foret, G., Garcia, O., Granados-Muñoz, M.J., Hannigan, J.W., Hase, F., Hassler, B., Huang, G., Hurtmans, D., Jaffe, D., Jones, N., Kalabokas, P., Kerridge, B., Kulawik, S., Latter, B., Leblanc, T., Le Flochmoën, E., Lin, W., Liu, J., Liu, X., Mahieu, E., McClure-Begley, A., Neu, J.L., Osman, M., Palm, M., Petetin, H., Petropavlovskikh, I., Querel, R., Rahpoe, N., Rozanov, A., Schultz, M.G., Schwab, J., Siddans, R., Smale, D., Steinbacher, M., Tanimoto, H., Tarasick, D.W., Thouret, V., Thompson, A.M., Trickl, T., Weatherhead, E., Wespes, C., Worden, H.M., Vigouroux, C., Xu, X., Zeng, G., Ziemke, J., 2018. Tropospheric Ozone Assessment Report: Present-day distribution and trends of tropospheric ozone relevant to climate and global atmospheric chemistry model evaluation. Elementa: Science of the Anthropocene 6, 39. https://doi.org/10.1525/elementa.291

Lu, X., Zhang, L., Zhao, Y., Jacob, D.J., Hu, Y., Hu, L., Gao, M., Liu, X., Petropavlovskikh, I., McClure-Begley, A., Querel, R., 2019. Surface and tropospheric ozone trends in the Southern Hemisphere since 1990: possible linkages to poleward expansion of the Hadley circulation. Science Bulletin 64, 400–409. https://doi.org/10.1016/j.scib.2018.12.021

McLinden, C.A., Fioletov, V., Krotkov, N.A., Li, C., Boersma, K.F., Adams, C., 2016. A Decade of Change in NO2 and SO2 over the Canadian Oil Sands As Seen from Space. Environ. Sci. Technol. 50, 331–337. https://doi.org/10.1021/acs.est.5b04985

Saunois, M., Stavert, A.R., Poulter, B., Bousquet, P., Canadell, J.G., Jackson, R.B., Raymond, P.A., Dlugokencky, E.J., Houweling, S., Patra, P.K., Ciais, P., Arora, V.K., Bastviken, D., Bergamaschi, P., Blake, D.R., Brailsford, G., Bruhwiler, L., Carlson, K.M., Carrol, M., Castaldi, S., Chandra, N., Crevoisier, C., Crill, P.M., Covey, K., Curry, C.L., Etiope, G., Frankenberg, C., Gedney, N., Hegglin, M.I., Höglund-Isaksson, L., Hugelius, G., Ishizawa, M., Ito, A., Janssens-Maenhout, G., Jensen, K.M., Joos, F., Kleinen, T., Krummel, P.B., Langenfelds, R.L., Laruelle, G.G., Liu, L., Machida, T., Maksyutov, S., McDonald, K.C., McNorton, J., Miller, P.A., Melton, J.R., Morino, I., Müller, J., Murguia-Flores, F., Naik, V., Niwa, Y., Noce, S., O'Doherty, S., Parker, R.J., Peng, C., Peng, S., Peters, G.P., Prigent, C., Prinn, R., Ramonet, M., Regnier, P., Riley, W.J., Rosentreter,

J.A., Segers, A., Simpson, I.J., Shi, H., Smith, S.J., Steele, L.P., Thornton, B.F., Tian, H., Tohjima, Y., Tubiello, F.N., Tsuruta, A., Viovy, N., Voulgarakis, A., Weber, T.S., van Weele, M., van der Werf, G.R., Weiss, R.F., Worthy, D., Wunch, D., Yin, Y., Yoshida, Y., Zhang, W., Zhang, Z., Zhao, Y., Zheng, B., Zhu, Qing, Zhu, Qiuan, Zhuang, Q., 2020. The Global Methane Budget 2000–2017. Earth System Science Data 12, 1561–1623. https://doi.org/10.5194/essd-12-1561-2020

Thompson, A.M., Stauffer, R.M., Wargan, K., Witte, J.C., Kollonige, D.E., Ziemke, J.R., 2021. Regional and Seasonal Trends in Tropical Ozone From SHADOZ Profiles: Reference for Models and Satellite Products. Journal of Geophysical Research: Atmospheres 126, e2021JD034691. https://doi.org/10.1029/2021JD034691

Ziemke, J.R., Chandra, S., Duncan, B.N., Froidevaux, L., Bhartia, P.K., Levelt, P.F., Waters, J.W., 2006. Tropospheric ozone determined from Aura OMI and MLS: Evaluation of measurements and comparison with the Global Modeling Initiative's Chemical Transport Model. Journal of Geophysical Research: Atmospheres 111. https://doi.org/10.1029/2006JD007089

Ziemke, J.R., Oman, L.D., Strode, S.A., Douglass, A.R., Olsen, M.A., McPeters, R.D., Bhartia, P.K., Froidevaux, L., Labow, G.J., Witte, J.C., Thompson, A.M., Haffner, D.P., Kramarova, N.A., Frith, S.M., Huang, L.-K., Jaross, G.R., Seftor, C.J., Deland, M.T., Taylor, S.L., 2019. Trends in global tropospheric ozone inferred from a composite record of TOMS/OMI/MLS/OMPS satellite measurements and the MERRA-2 GMI simulation. Atmospheric Chemistry and Physics 19, 3257–3269. https://doi.org/10.5194/acp-19-3257-2019

Figures:

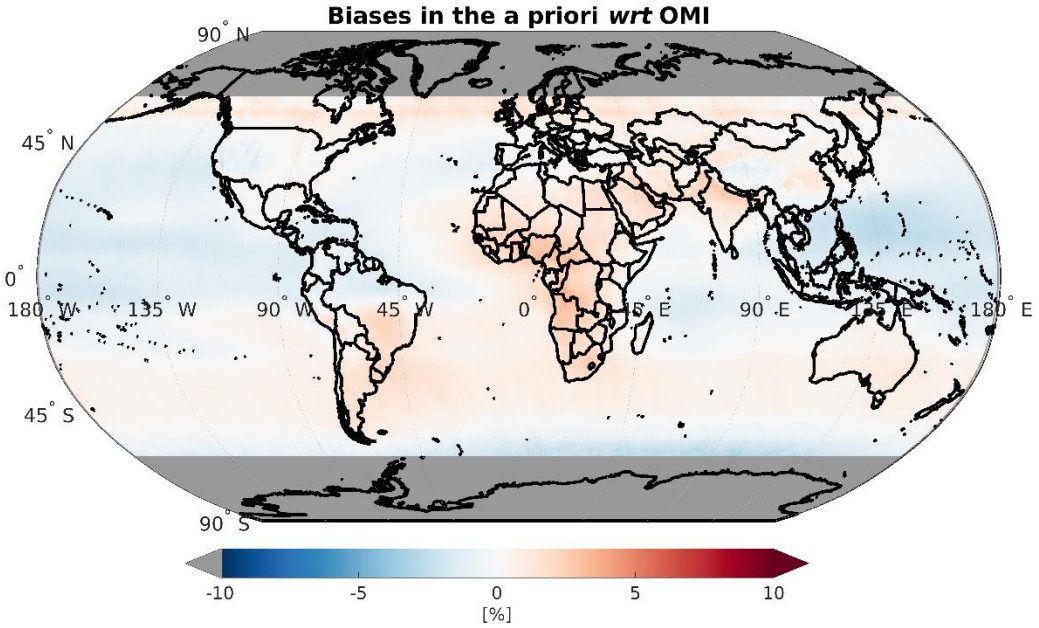

Figure S1. The relative biases in MERRA2-GMI total ozone columns with respect to OMI total columns OMTO3 (data obtained from https://disc.gsfc.nasa.gov/datasets/OMTO3_003/summary).

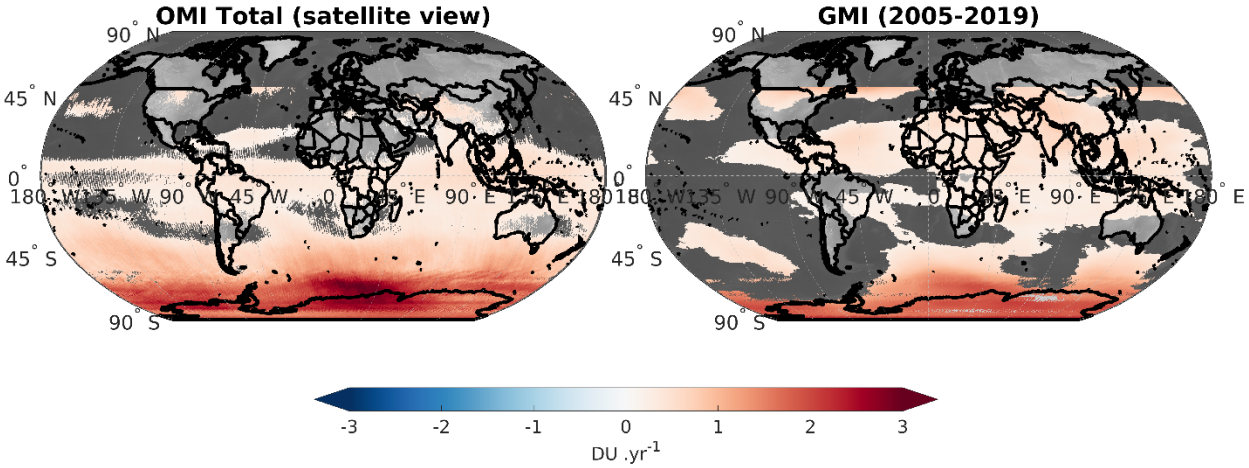

Figure S2. The linear trend of total ozone columns from OMTO3 and MERRA2GMI in 2005-2019.

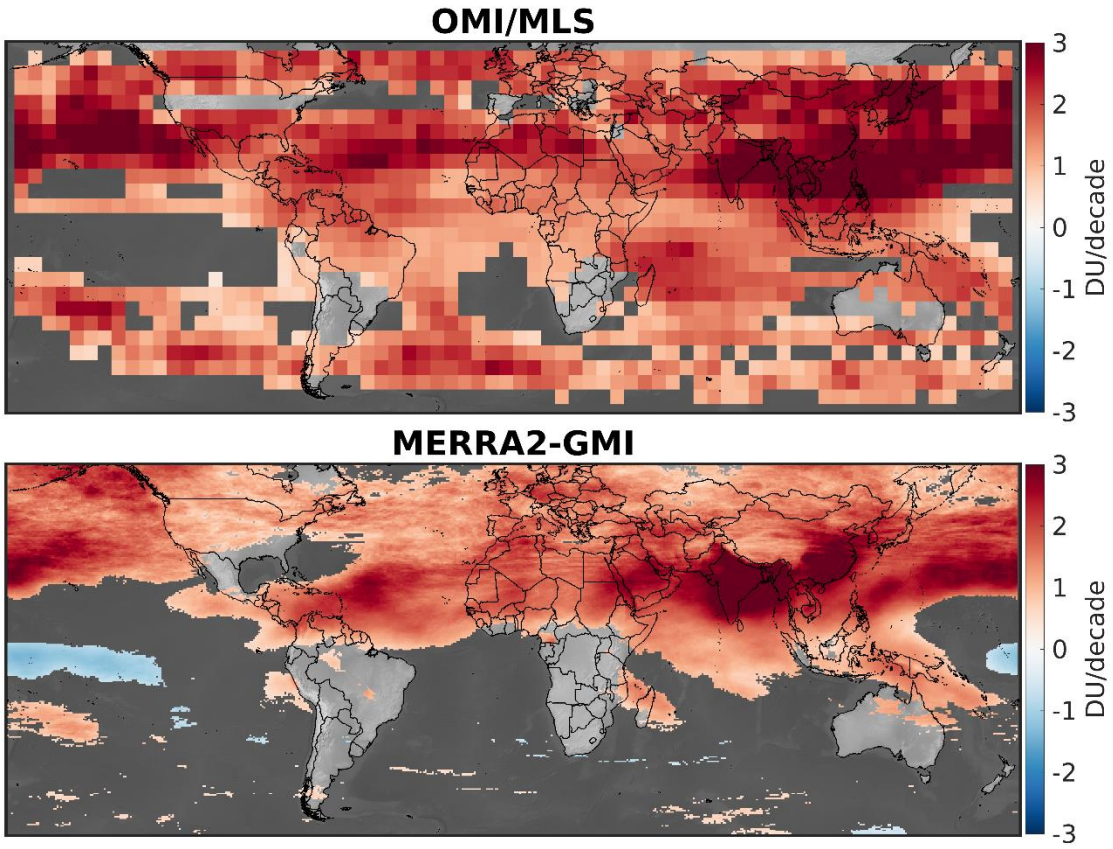

Figure S3. The global maps of statistically significant linear trends of tropospheric ozone columns observed by OMI/MLS and simulated by MERRA2-GMI in 2005-2019.

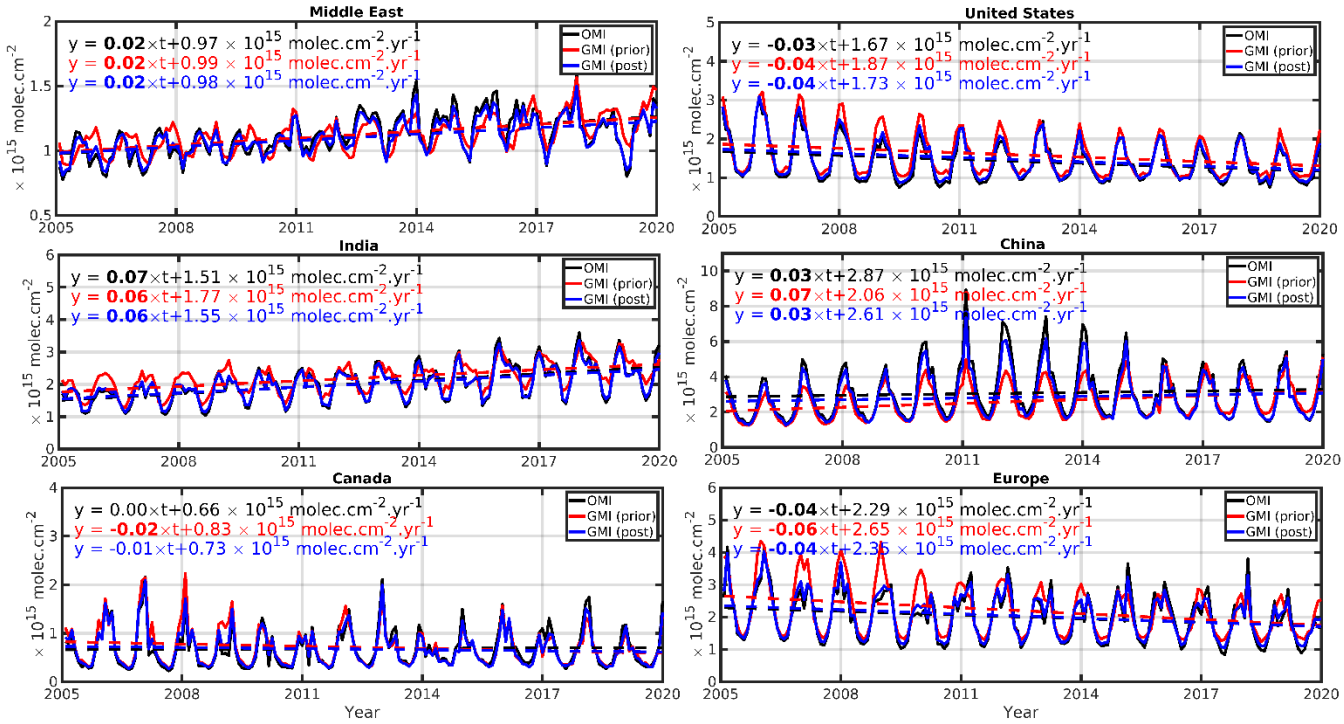

Figure S4. The long-term series of tropospheric NO_2 columns derived from OMI, MERRA2-GMI before and after taking the OI corrections factors into consideration for various regions around the world. The linear trends are applied along with a seasonal cycle. Statistically significant trends are highlighted by bold fonts.

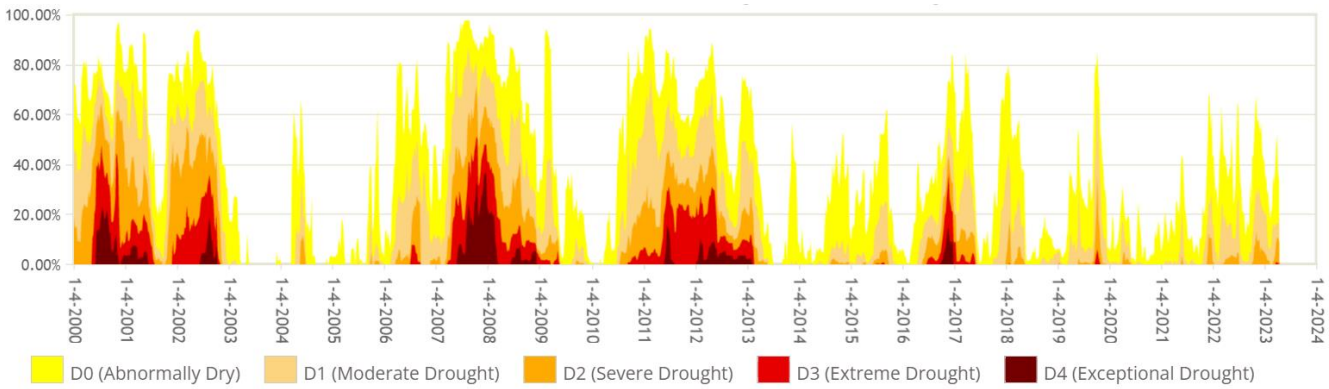

Figure S5. Southeast percent area in U.S. drought monitor categories derived from https://droughtmonitor.unl.edu/DmData/TimeSeries.aspx. The U.S. Drought Monitor is jointly produced by the National Drought Mitigation Center at the University of Nebraska-Lincoln, the United States Department of Agriculture, and the National Oceanic and Atmospheric Administration. Plot courtesy of NDMC.

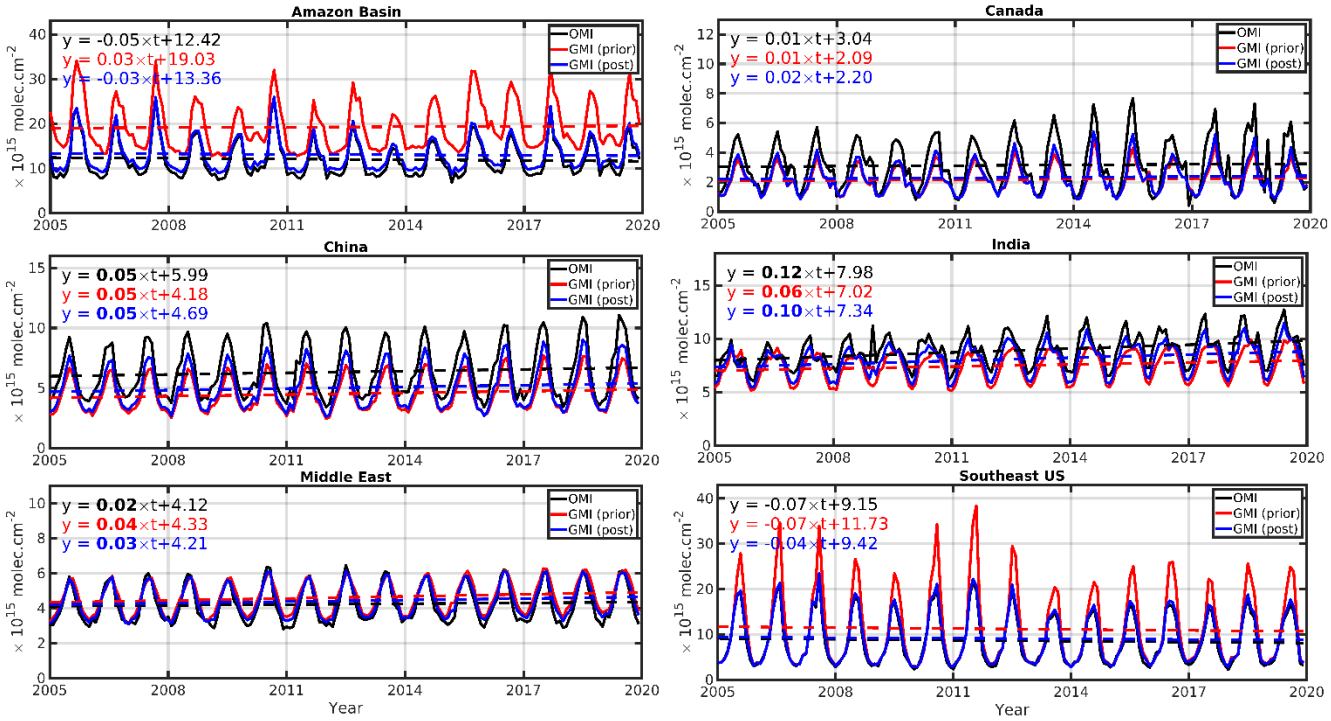

Figure S6. Same as Figure S4 but for HCHO.

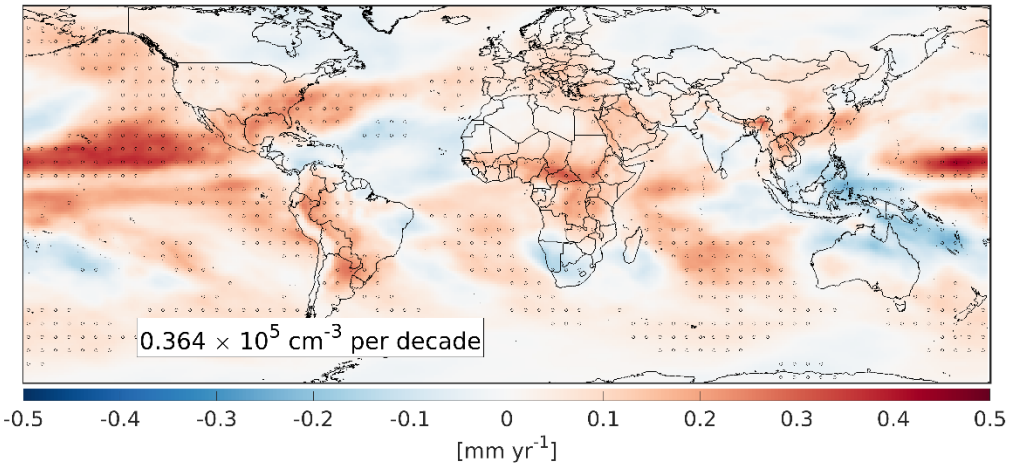

Figure S7. The linear trends of simulated IWV by our GEOS run. The ENSO effect is not considered in the trend analysis.

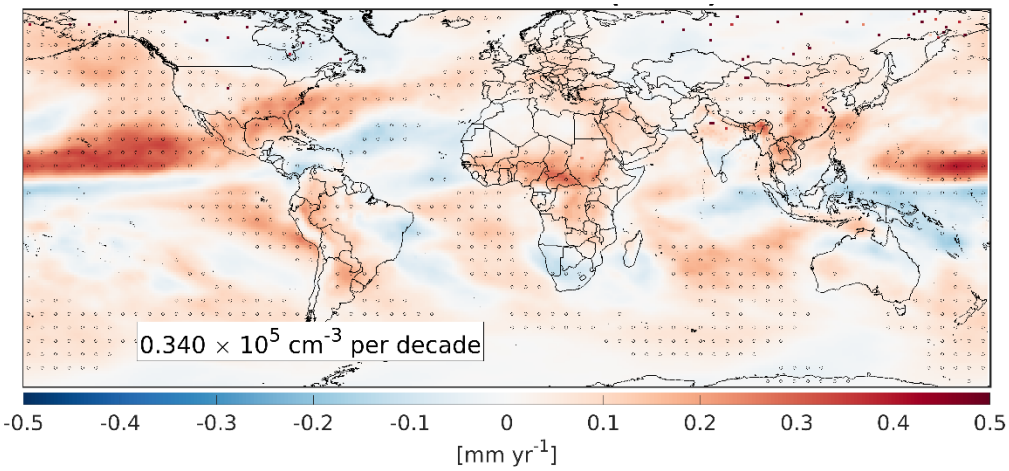

Figure S8. Same as Figure S7 but the ENSO effect is considered.

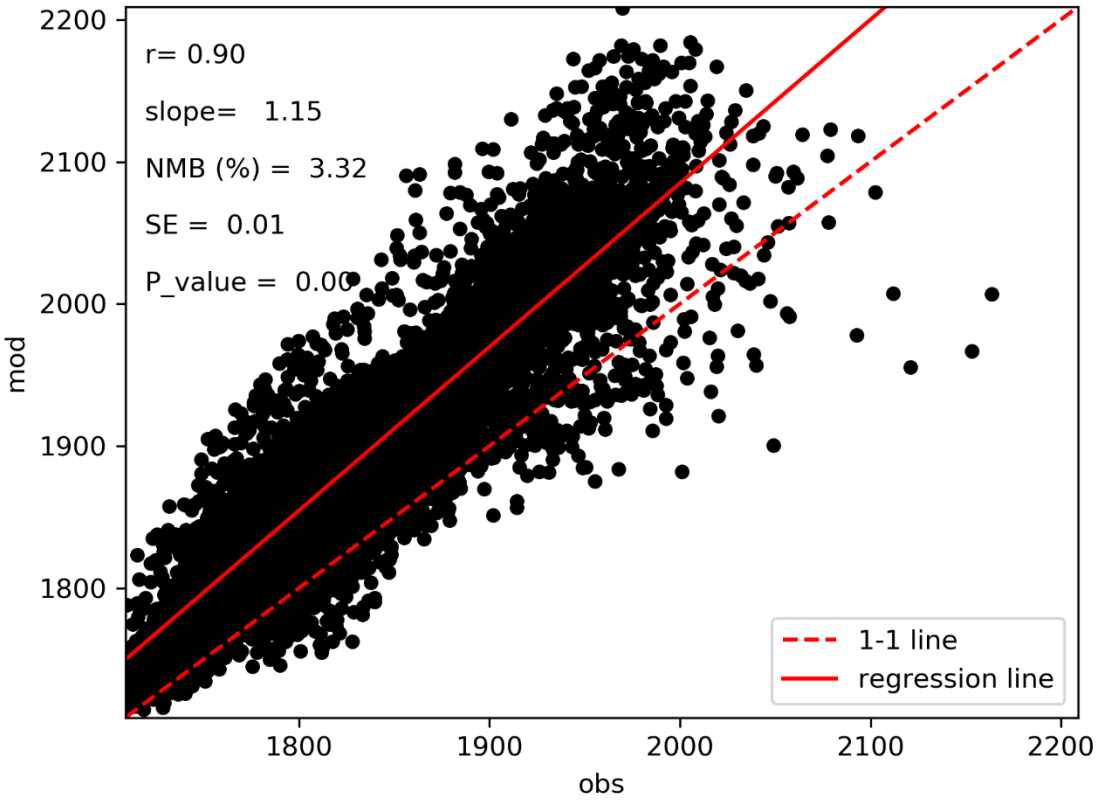

Figure S9. The scatter plot of CH_4 concentrations simulated by our GEOS-quickchem model based on *Sanalysis* (y-axis) contrasted by those observed by NOAA flasks surface observations (x-axis). The sampling size is monthly.

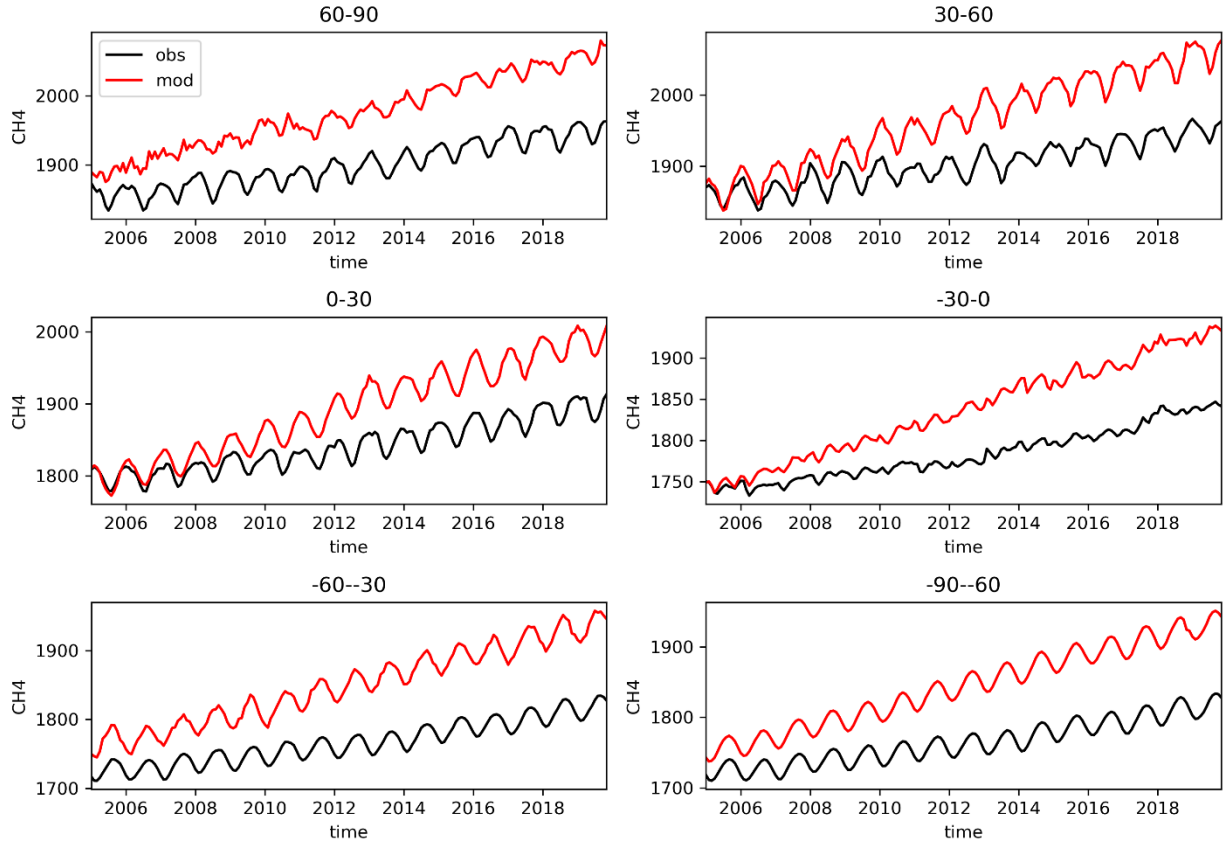

Figure S10. The zonal-averaged CH_4 concentrations simulated by our GEOS-quickchem model based on *Sanalysis* (red curves) and observed by NOAA flasks surface observations from 2005 till 2020.

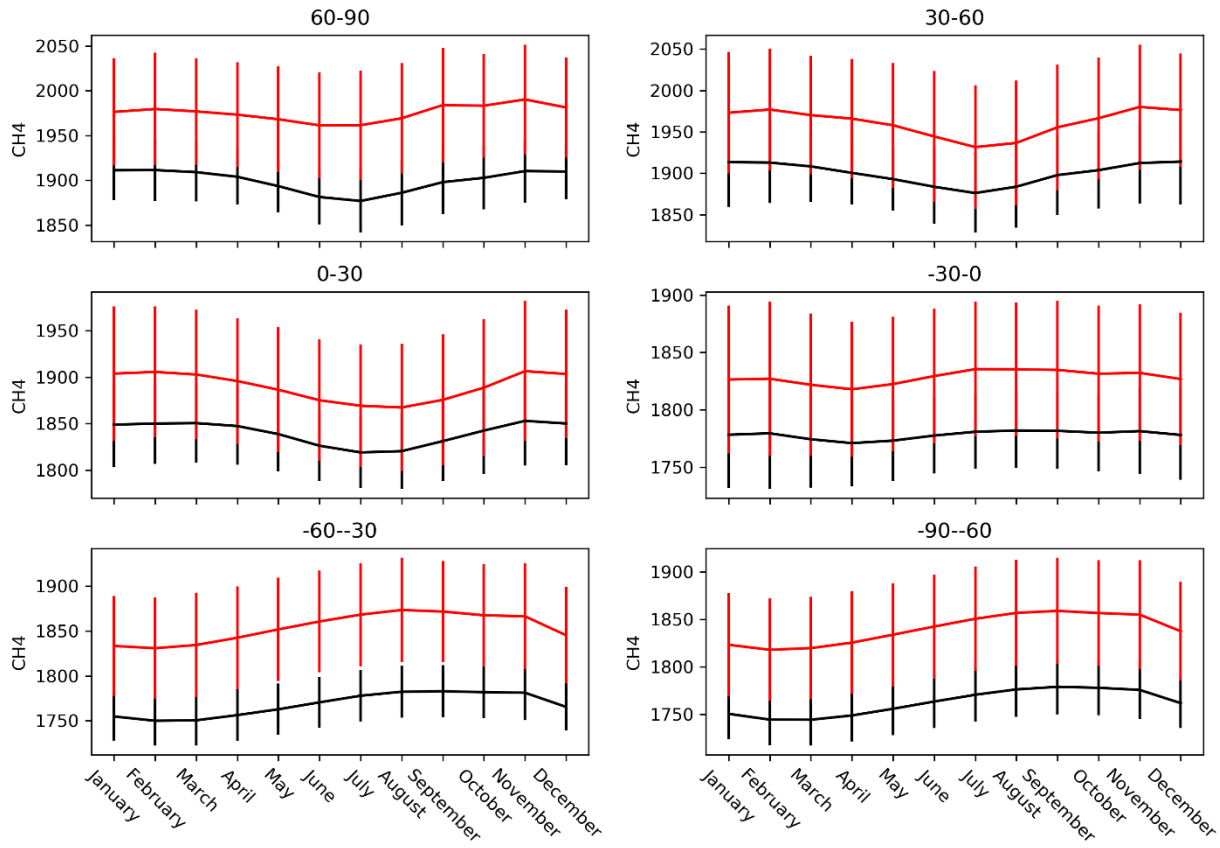

Figure S11. The zonal-averaged seasonal pattern of CH_4 concentrations simulated by our GEOS-quickchem model based on *Sanalysis* (red curves) and observed by NOAA flasks surface observations. All data from 2005 till 2020 are used to make this plot.

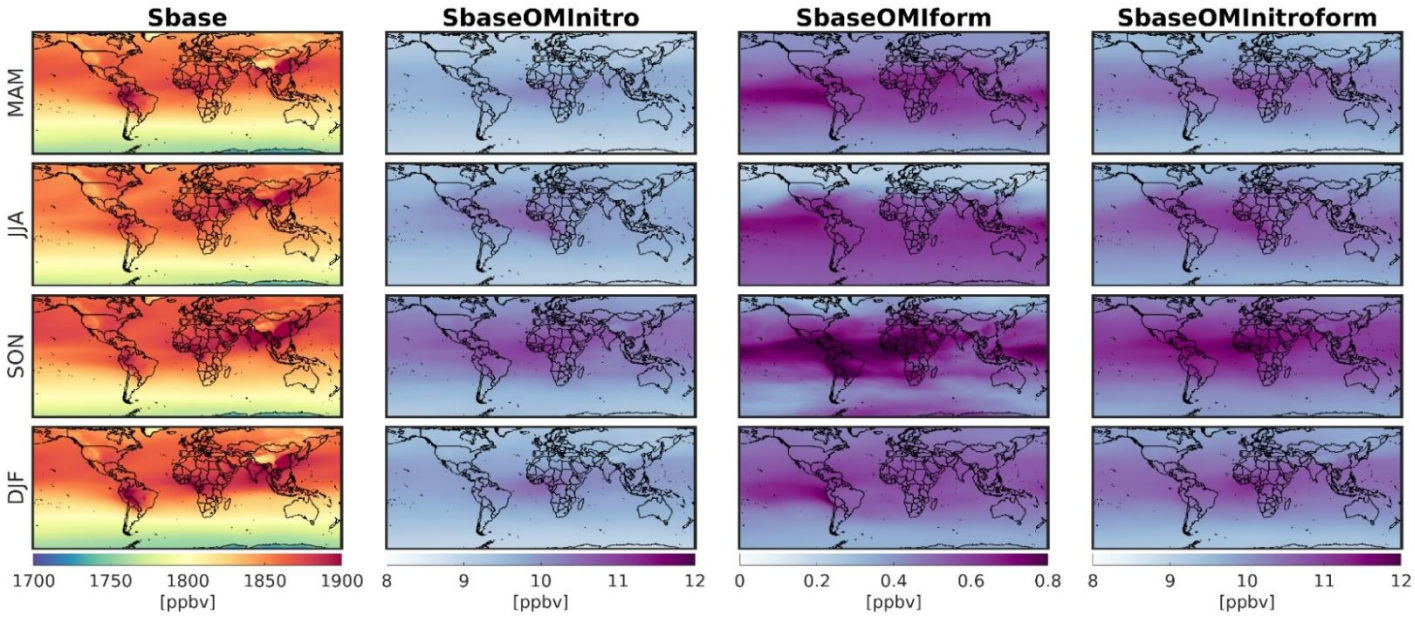

Figure S12. (first column) simulated XCH_4 from *Sanalysis* experiment in different seasons, (second to fourth columns) the XCH_4 changes due to adjustments made by OMI NO_2 (*SOMInitro*), OMI HCHO (*SOMIform*), and both (*SOMInitroform*).

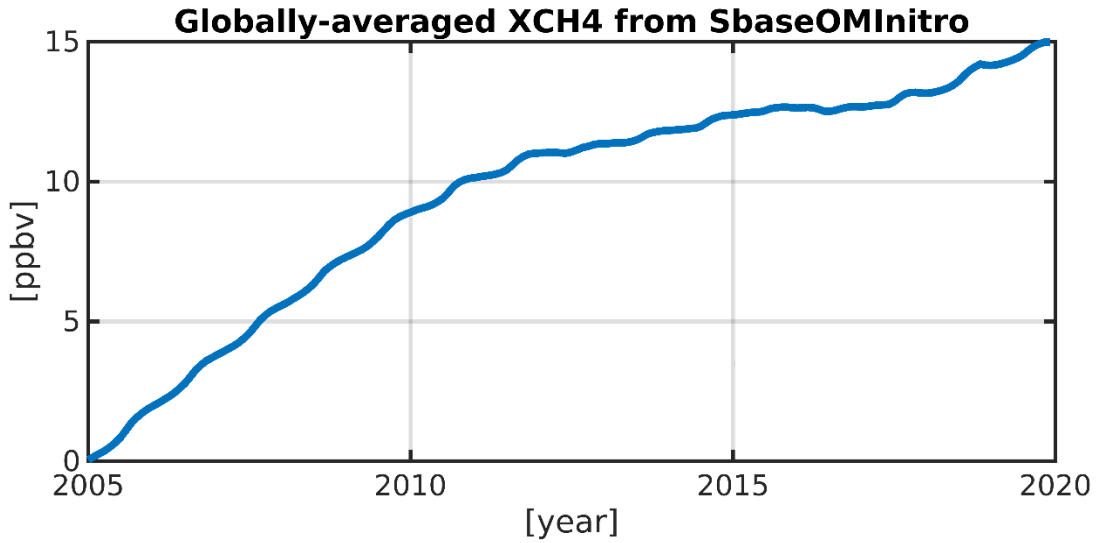

Figure S13. The global time series of XCH_4 differences induced by adjustments suggested by OMI tropospheric NO_2 columns (i.e., *SOMInitro*).

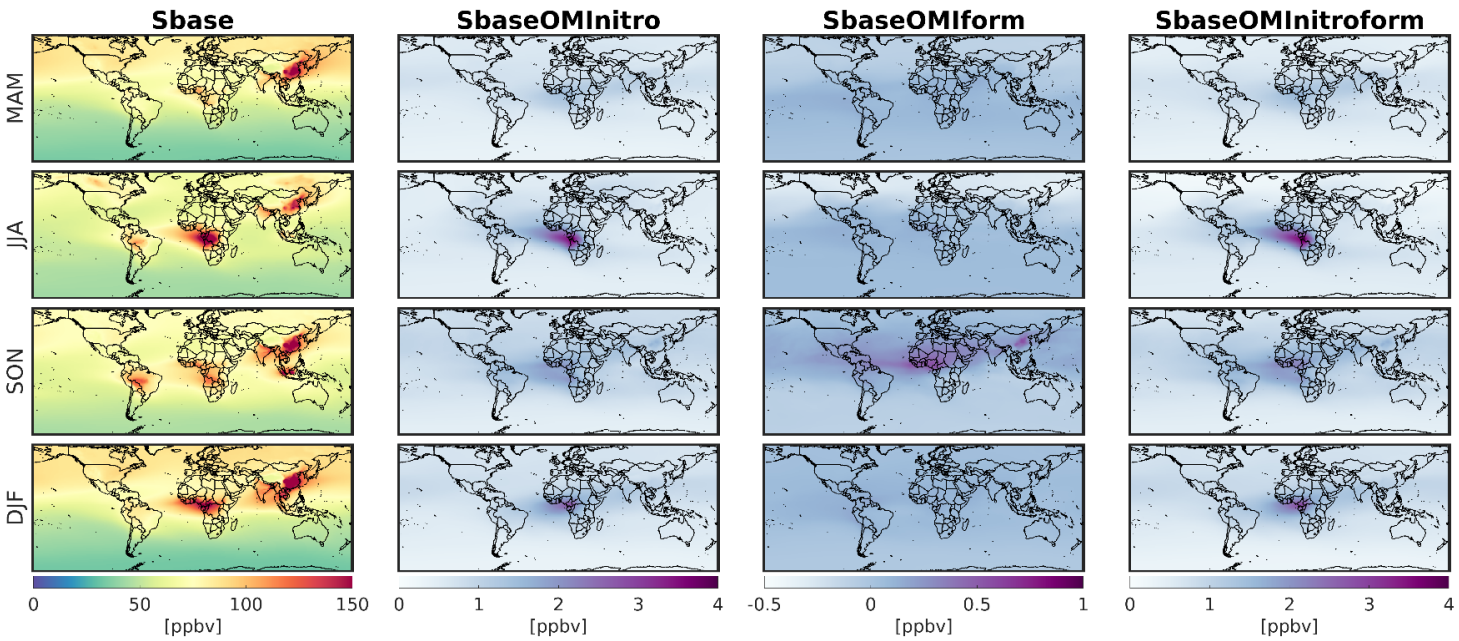

Figure S14. Same as Figure S12 but for XCO.

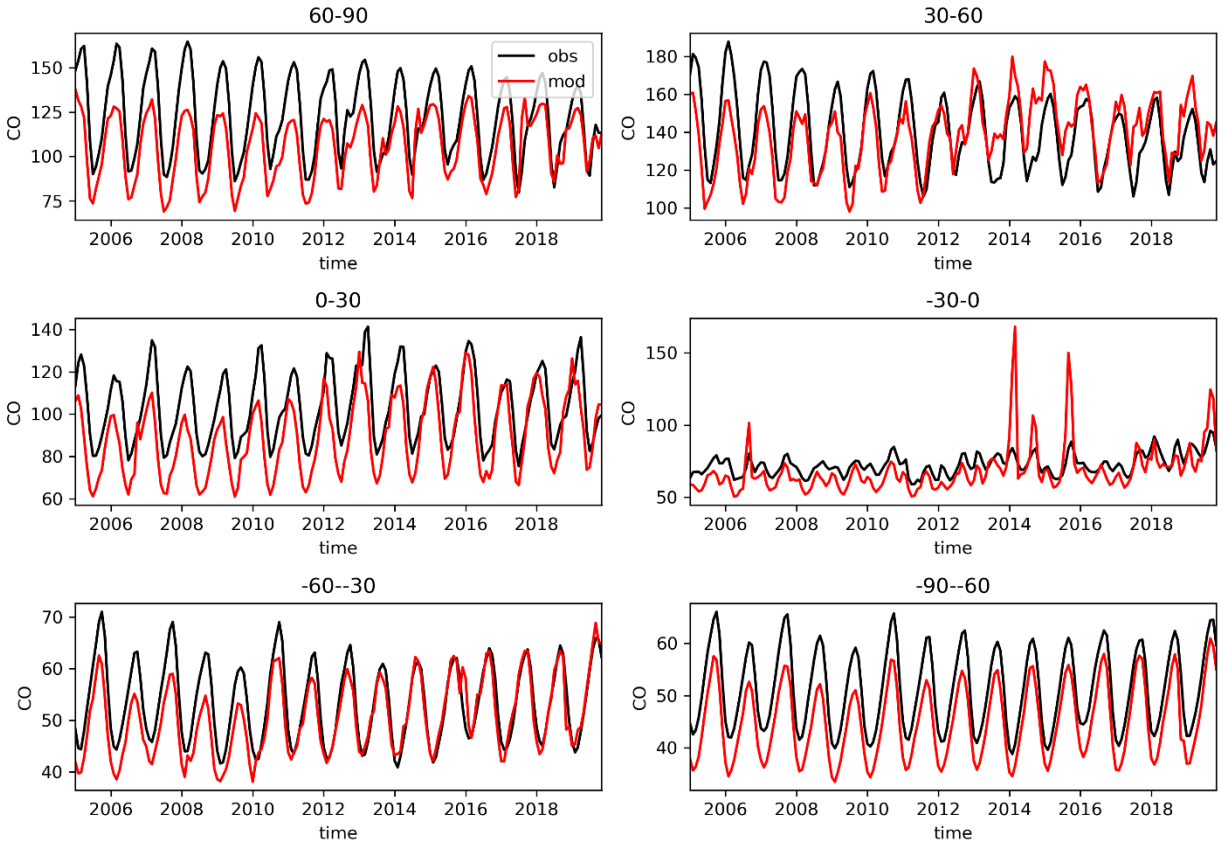

Figure S15. Same as Figure S10 but for surface CO.

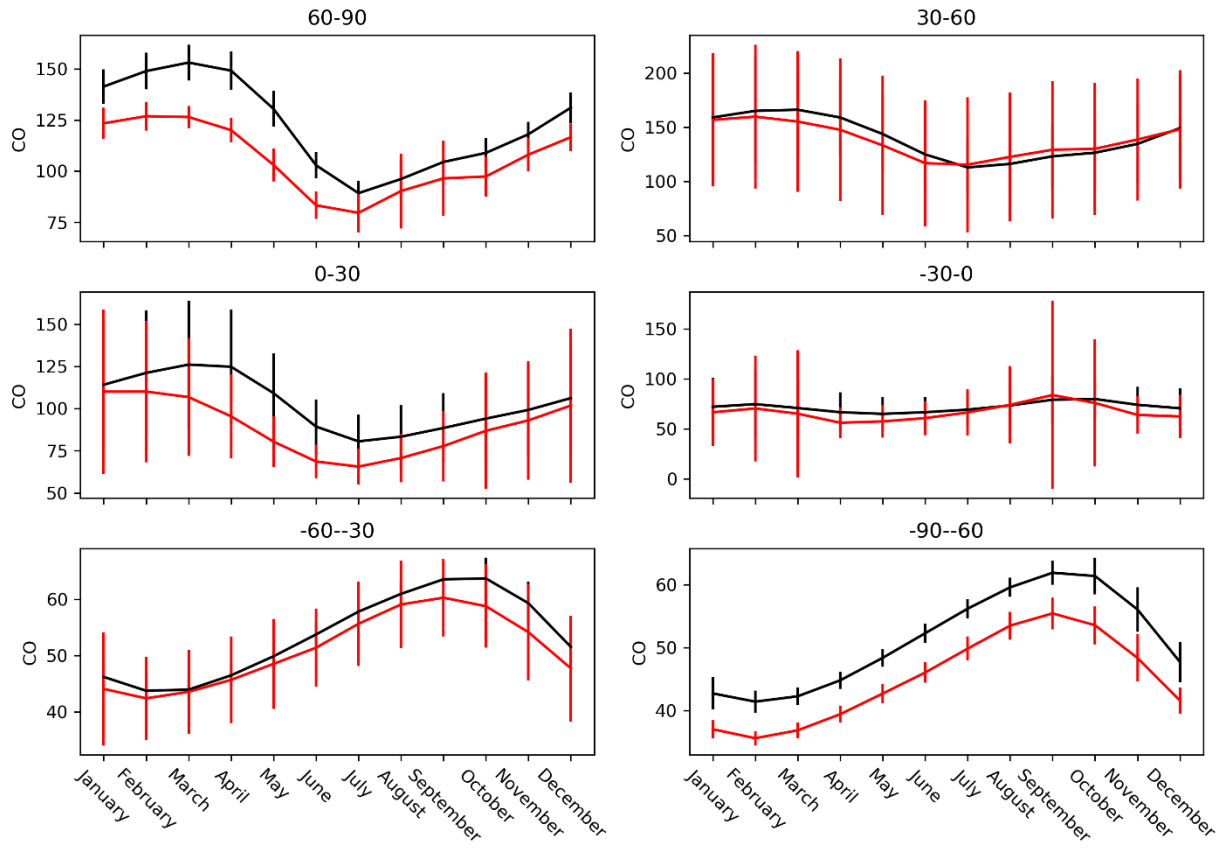

Figure S16. Same as Figure S11 but for CO.

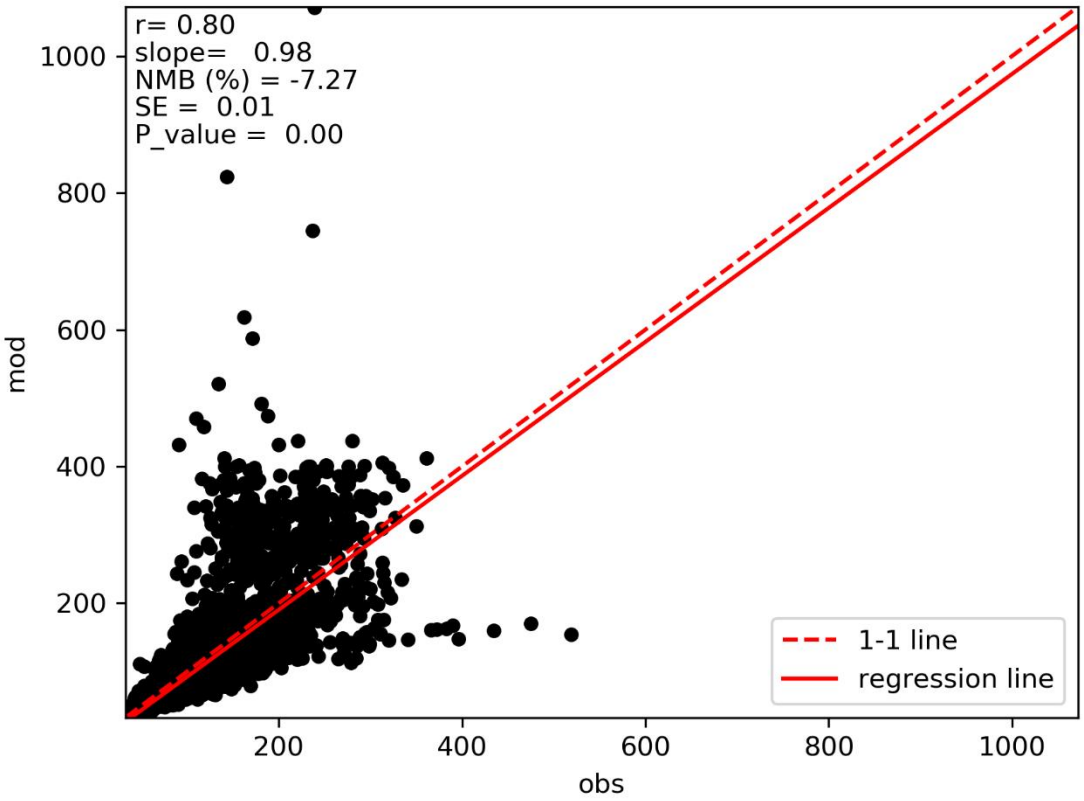

Figure S17. The scatter plot of CO concentrations simulated by our GEOS-quickchem model based on *Sanalysis* (y-axis) contrasted by those observed by NOAA flasks surface observations (x-axis). The sampling size is monthly.

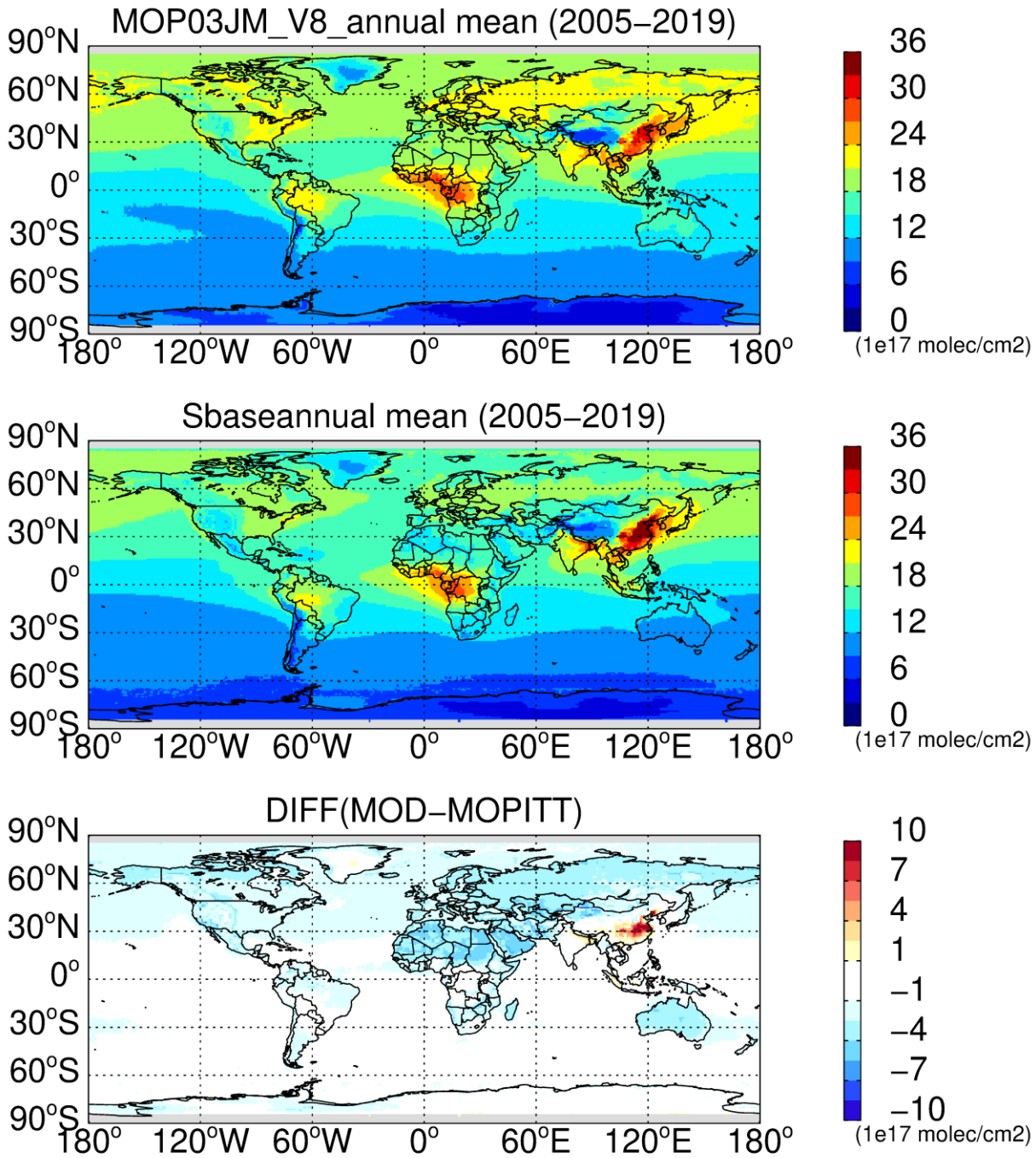

Figure S18. (top) contour maps of MOPITT total CO columns in 2005-2019, (middle) simulated total CO columns based on *Sanalysis*, and (bottom) their differences. The averaging kernels from the retrieval algorithm have been applied to the model results.

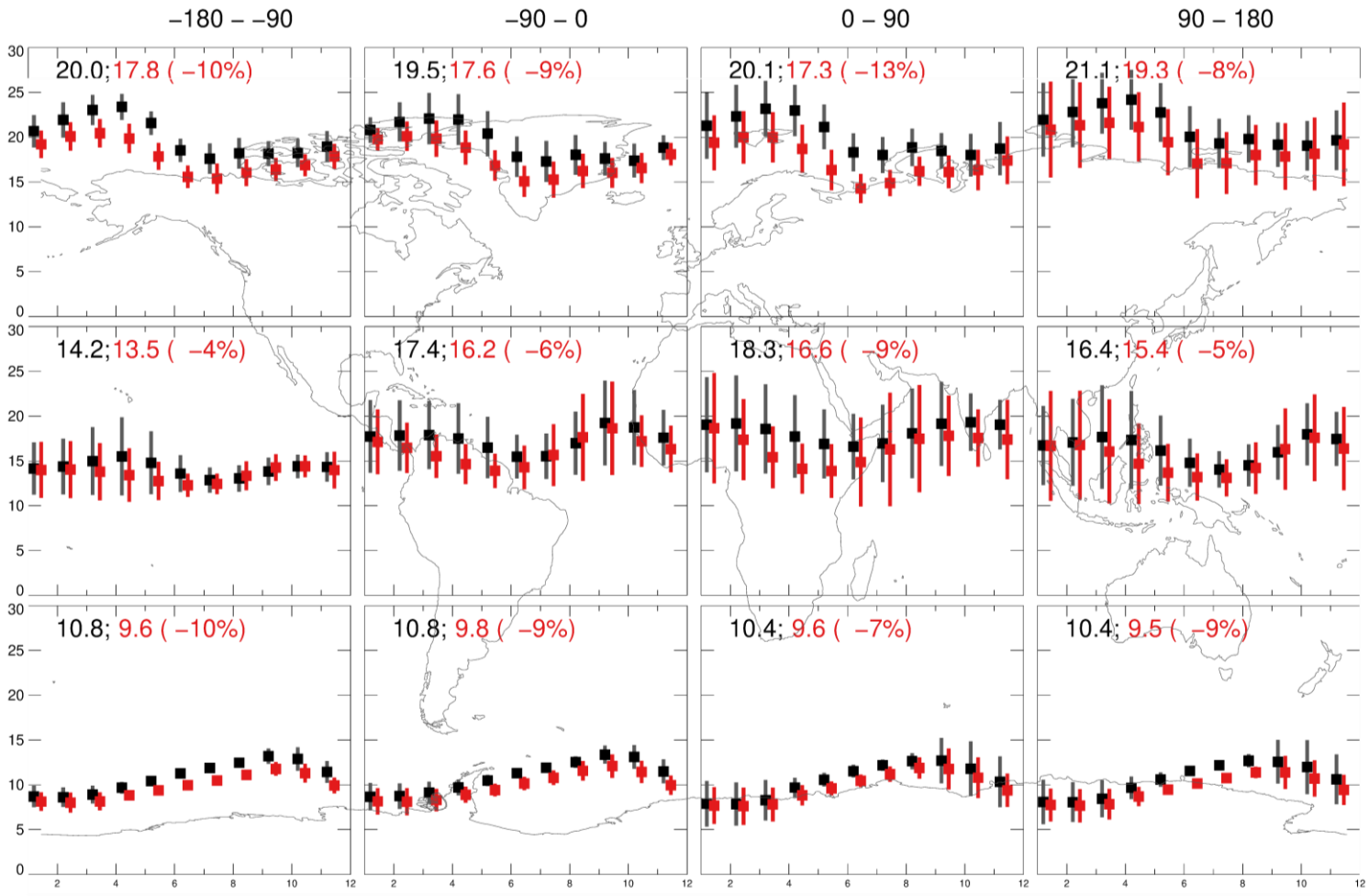

Figure S19. The zonally-averaged seasonal cycles between *Sanalysis* CO total columns and those of MOPITT.

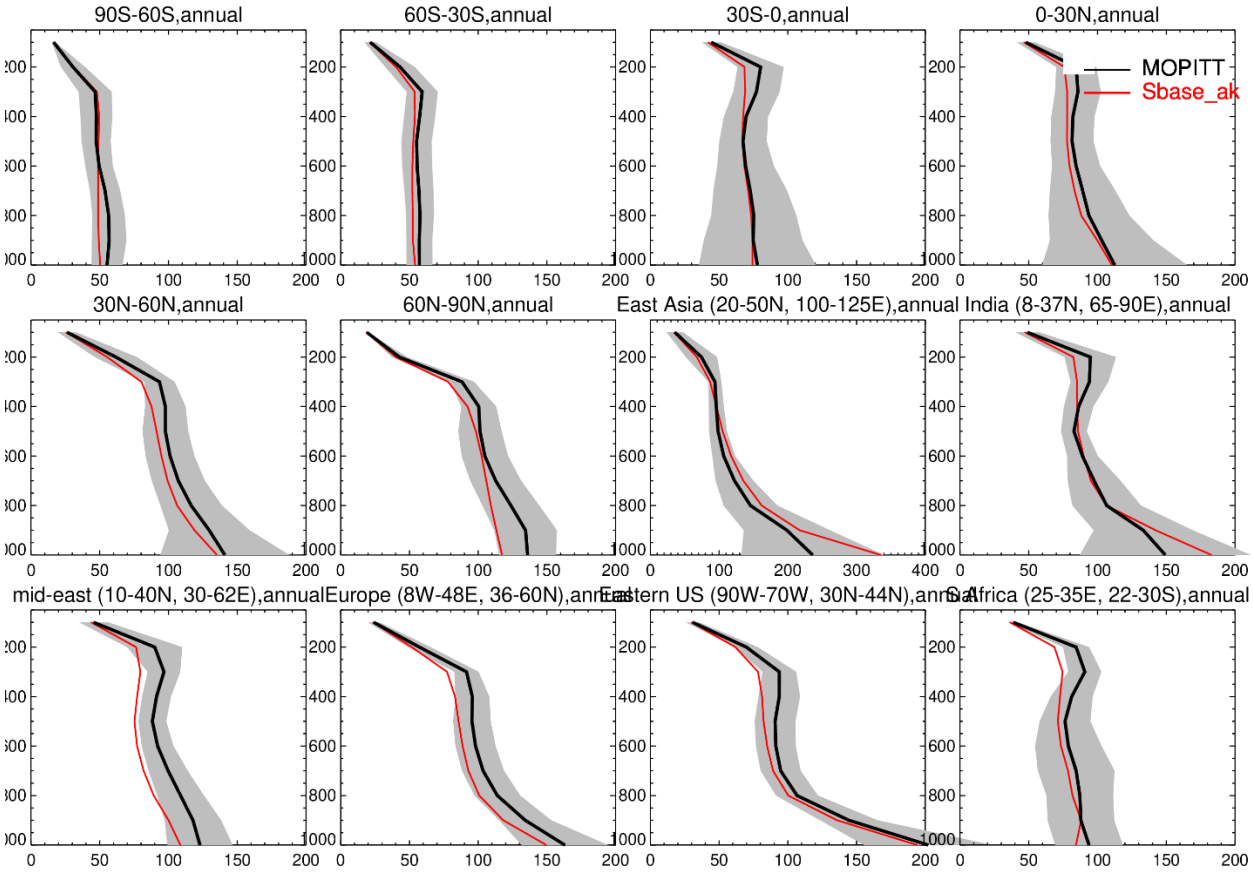

Figure S20. The zonally-averaged vertical distribution of CO simulated by *Sanalysis* and retreived by MOPITT. The averaging kernels are considered.

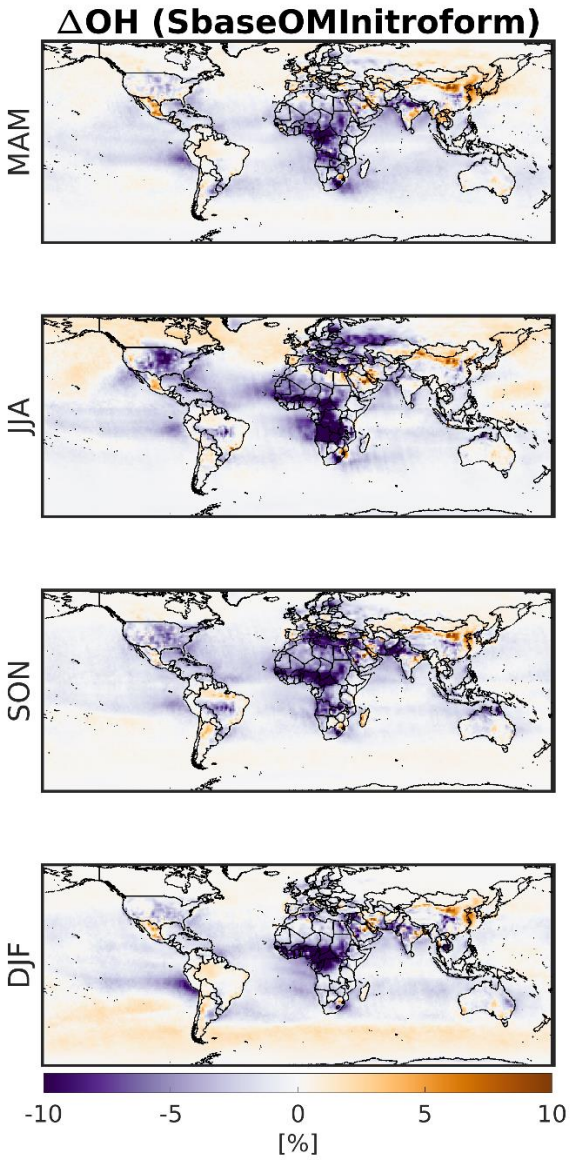

Figure S21. The effect of OMI NO_2 and HCHO adjustments on TOH.

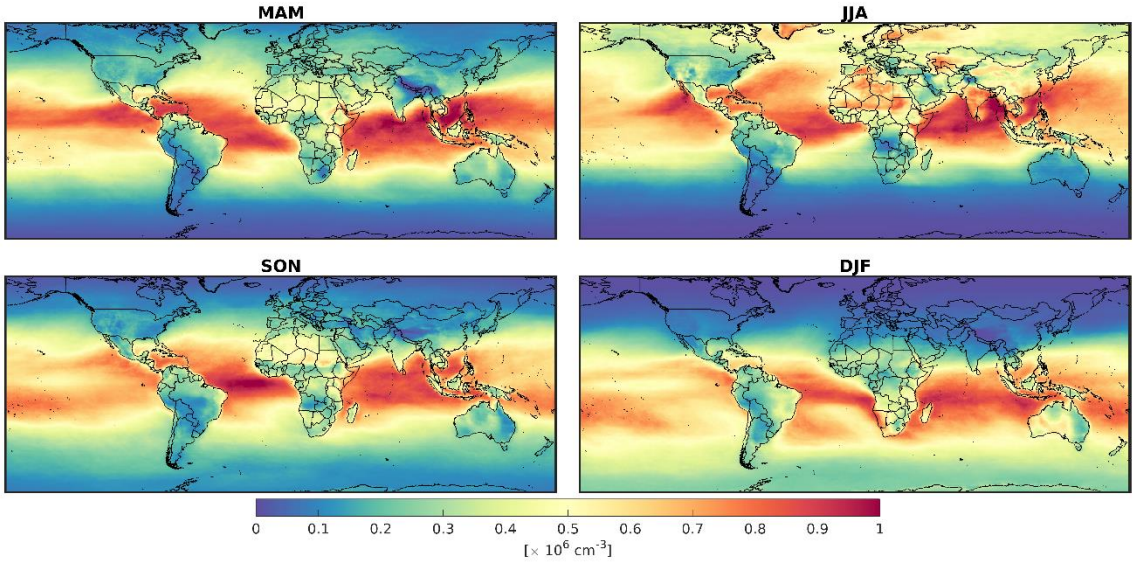

Figure S22. The semi-normalized response of tropospheric OH to tropospheric water vapor changes based on ECCOH offline calculations in 2012.

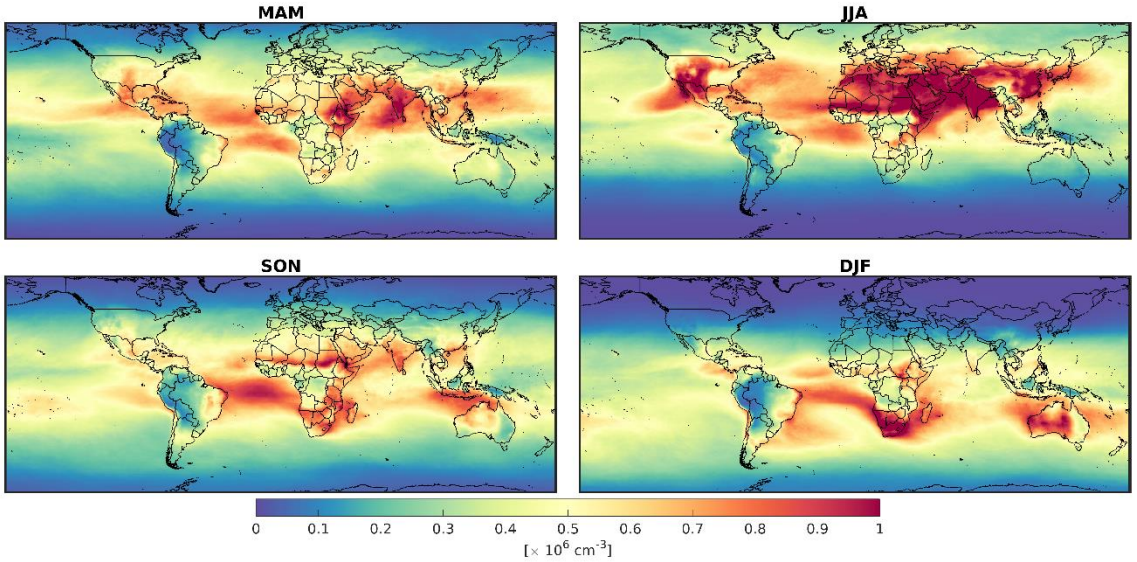

Figure S23. The semi-normalized response of tropospheric OH to tropospheric ozone changes based on ECCOH offline calculations in 2012.

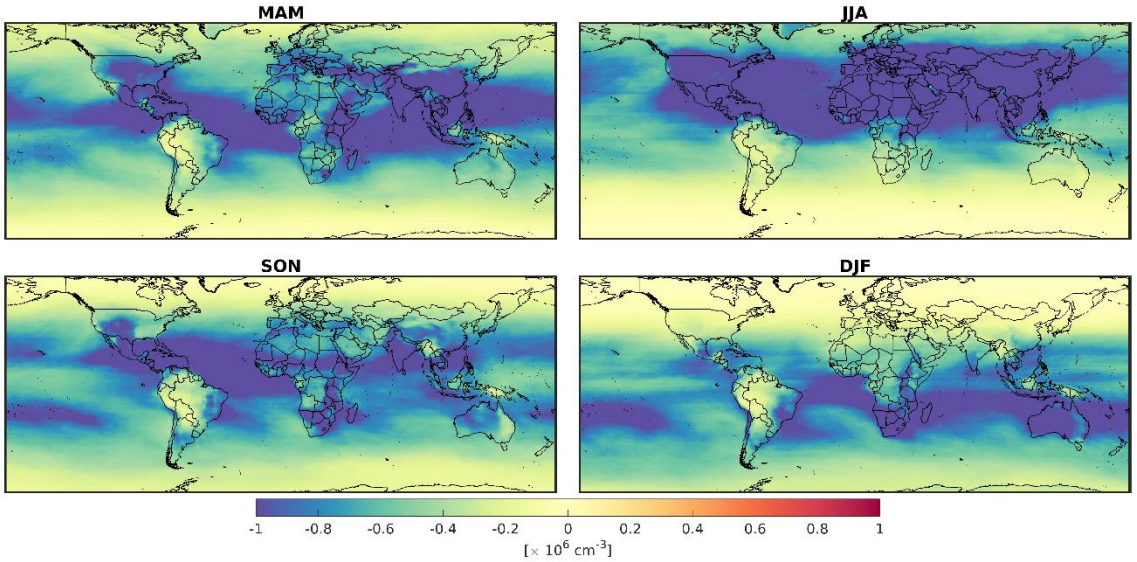

Figure S24. The semi-normalized response of tropospheric OH to stratospheric column changes based on ECCOH offline calculations in 2012.

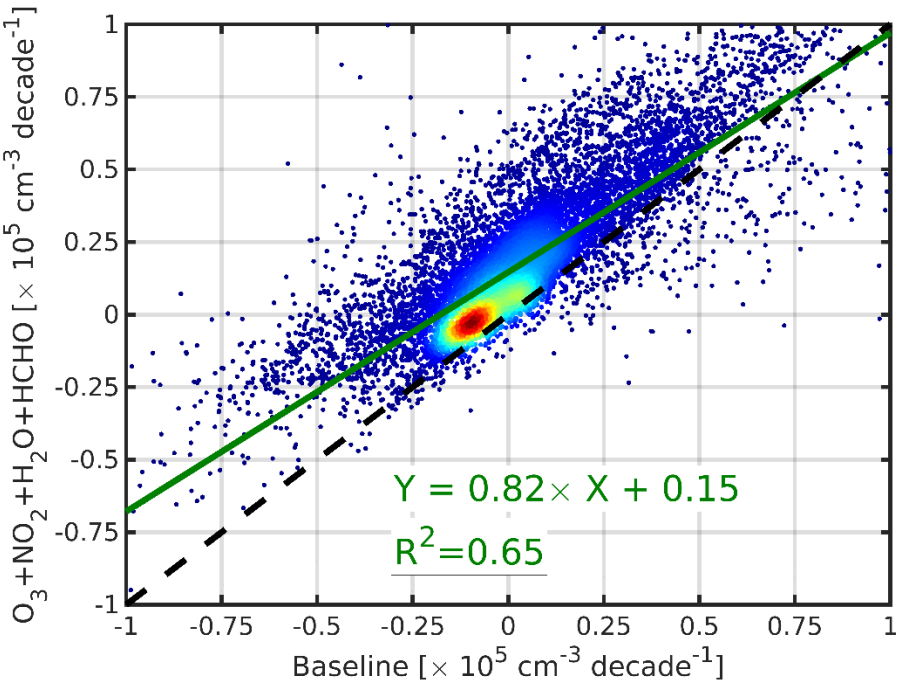

Figure S25. The comparison of the baseline (*Sanalysis*) with varying OH drivers (x-axis) against the sum of five experiments designed to isolate the effect of each OH driver on OH trends (y-axis).